Published by IOP Publishing for Sissa Medialab

Received: *September 2, 2019*
Revised: *December 6, 2019*
Accepted: *January 3, 2020*
Published: *February 20, 2020*

21st International Workshop on Radiation Imaging Detectors
7–12 July 2019
Crete, Greece

Discrimination of benign and malignant microcalcifications using dual-energy imaging

H. Kim,[a] **M. Lee,**[b] **D. Kim**[b] **and H.-J. Kim**[a,b,1]

[a] *Department of Radiological Science, College of Health Science, Yonsei University, 1 Yonseidae-gil, Wonju, Gangwon, 220-710 Republic of Korea*
[b] *Department of Radiation Convergence Engineering, College of Health Science, Yonsei University, 1 Yonseidae-gil, Wonju, Gangwon, 220-710 Republic of Korea*

E-mail: hjk1@yonsei.ac.kr

Abstract: Screening mammography has a high detection efficiency for microcalcifications. In a mammogram, morphological characteristics are used to distinguish benign and potentially malignant changes. In this study, we propose a new method to distinguish malignant and benign microcalcifications using only mammographic images based on the dual-energy method. A photon-counting spectral mammography system was simulated using the Geant4 Application for Tomographic Emission (GATE) simulation tool. The dual-energy images were obtained using two energy bins. Microcalcifications of type I (calcium oxalate) and type II (calcium hydroxyapatite) were studied. For statistical analysis, the microcalcifications were classified as type I or type II based on a score calculated using the dual-energy images. The score values were calculated using the ratio of values at low energy and high energy because the attenuation difference was small in the high-energy region and large in the low-energy region. In other words, the classification of microcalcifications associated with pathogenesis was performed using the attenuation ratio as a discrimination criterion. For the appropriate dual-energy images, the effects on the energy spectra of microcalcifications were evaluated. We confirmed that the contrast and the noise were affected because the classification method used in this study is based on the pixel values of the images. In addition, we suggested the possibility of automatic classification for malignant microcalcifications using segmentation methods and the minimum and maximum thresholds of score values.

Keywords: X-ray mammography and scinto- and MRI-mammography; X-ray radiography and digital radiography (DR)

[1] Corresponding author.

https://doi.org/10.1088/1748-0221/15/02/C02033

Contents

2020 JINST 15 C02033

1 Introduction

Breast microcalcifications are present in approximately 30% of all malignant breast lesions [1], and screening mammography has a high detection efficiency for microcalcifications. There are well-described patterns that help to distinguish between benign and potentially malignant changes in mammography. The current approaches for interpretation include the characteristics of the extent, morphology, and distribution of the calcifications [2, 3]. As new approach, we propose a method to distinguish between malignant and benign microcalcifications using mammographic images based on the dual-energy method. In previous studies, Kim et al. [4] evaluated the feasibility of microcalcification classification using dual-energy method according to combinations of energy spectra and various breast phantoms. In this study, the effects on the position and width of the energy range in the low-energy region were evaluated to improve classification performance. Furthermore, we propose an improved method for the automatic detection of malignant lesions using the scores obtained with the dual-energy method.

Two types of microcalcifications were investigated in this study: type I consists of calcium oxalate dihydrate (CaC_2O_4–$2H_2O$) or weddellite, which is commonly found in benign ductal cysts. Type II deposits consist of calcium phosphates, specifically calcium hydroxyapatite ($Ca_5(PO_4)_3(OH)$). Type II microcalcifications are associated with benign and malignant lesions, and their presence usually indicates signs of malignant breast cancer [5, 6]. Therefore, quantitative analysis criteria are needed to distinguish two types of microcalcifications depending on their chemical composition in mammograms. In this study, spectral mammography based on a photon-counting detector (PCD) was used. The PCD system can measure the photon energy deposited

in each event using application-specific integrated circuits (ASIC), thereby providing useful spectral information. The energy discrimination capabilities enable the acquisition of energy-resolved images in a single exposure [7]–[9]. By setting the appropriate threshold energy, the quantitative identification of microcalcifications can be performed effectively.

2 Materials and methods

2.1 Simulation set-up

We modeled a photon-counting spectral mammography system using the Geant4 Application for Tomographic Emission (GATE) simulation tool. The detector used CdZnTe (CZT) material, characterized by high quantum efficiency with a low thickness [10]. The dimensions of the detector were 25.6 mm × 25.6 mm × 1 mm, and the pixel pitch was 0.1 mm × 0.1 mm. The detector contained 256 × 256 pixels.

We simulated two breast phantoms: a simple-shaped breast phantom with a homogeneous background and an extended cardiac-torso (XCAT) phantom with a heterogeneous background. The thickness of the simple-shaped breast phantom was 3 cm, and it had a 50/50 ratio for the adipose/glandular tissue. The XCAT phantom is an excellent tool to study the effects of anatomy and patient motion. This phantom was generated from dedicated breast CT data of several human subjects by post-processing and segmenting them into skin, adipose tissue, and fibroglandular tissues according to density, which can be compressed to various thicknesses [11, 12]. In this study, we simulated the XCAT breast phantom [13] compressed to 3 cm with a heterogeneous background. The pixel array of the XCAT phantom was 256 × 256, and the pixel pitch was 1 mm × 1 mm. Microcalcifications were used as type I (calcium hydroxyapatite, $Ca_5(PO_4)_3(OH)$, denoted as HA) and type II (calcium oxalate, CaC_2O_4, denoted as CO) for malignant and benign microcalcifications, respectively [5, 6]. Furthermore, these sizes ranging from 150–550 μm were embedded in the two simulated breast phantoms. The microcalcification sample images were randomly obtained for various sizes and locations: 230 images of the simple-shaped phantom and 60 images of the XCAT phantom.

2.2 Dual-energy method

The energy spectrum was obtained using a combination of a tungsten anode and an Al filter of thickness 2 mm. Spectra were acquired using the Tungsten Anode Spectral Model using Interpolating Polynomials (TASMIP) X-ray spectral model [14]. In addition, two energy bins were used to obtain dual-energy images. The simulated detector signal S has the following form [4, 5]:

$$S_{\text{calc}} = \int_0^\infty I_0(E)\, e^{-\left(\mu_a(E_i)l_a + \mu_g(E_i)l_g + \mu_c(E_i)l_c\right)} Q_i(E)\, dE, \tag{2.1}$$

$$S_{\text{backg}} = \int_0^\infty I_0(E)\, e^{-\left(\mu_a(E_i)l_a + \mu_g(E_i)l_g\right)} Q_i(E)\, dE, \tag{2.2}$$

$$D_l = \ln\left(\frac{S^l_{\text{backg}}}{S^l_{\text{calc}}}\right), \qquad D_h = \ln\left(\frac{S^h_{\text{backg}}}{S^h_{\text{calc}}}\right), \tag{2.3}$$

$$\text{Score} = D_l / D_h. \tag{2.4}$$

2020 JINST 15 C02033

The parameter I_0(E) represents the blank scan energy spectrum, and i is one of the two energy bins (low or high). The parameters μ_a, μ_g, and μ_c represent the linear attenuation coefficients of adipose tissues, glandular tissues, and the two types of microcalcifications, respectively. The parameters l_a, l_g, and l_c represent the propagation path lengths of X-rays through adipose tissues, glandular tissues, and the two types of microcalcifications, respectively. The parameter Q_i is the efficiency of the detector; the simulation was performed assuming an ideal detector with high efficiency. The parameters S_{backg} and S_{calc} were estimated from the pixels near the microcalcification and microcalcification pixels, respectively. Subsequently, the logarithmic signal function D_i was calculated for the low- and high-energy bins. It was assumed that the pixel values in the microcalcification region and their neighboring pixels were only affected by the attenuation of microcalcifications. For statistical analysis, the microcalcifications were classified as either HA or CO based on the calculated score. The score values were calculated using the ratio of values at low energy and high energy because the attenuation difference was small in the high-energy region and large in the low-energy region.

2.3 Image analysis

The contrast-to-noise ratio (CNR) for microcalcification was used to set the appropriate low-energy region. This parameter was calculated using the following equation [15].

$$\text{CNR} = \frac{|S_C - S_B|}{\sqrt{\sigma_C^2 + \sigma_B^2}} \tag{2.5}$$

where S_C and S_B are the mean values of the microcalcification region and the breast region, respectively; σ_C and σ_B are the standard deviations in the microcalcification region and the breast region, respectively.

To evaluate the performance of classification, area-under-the-ROC-curve (AUC) assessments were performed. The AUC was calculated using the Wilcoxon-Mann-Whitney statistic nonparametric method [16]. Furthermore, a binary classification task with m and n samples was considered. We denoted the scores of the calcium oxalate samples by $x_1, \ldots, x_n$ and the scores of the calcium hydroxyapatite samples by $y_1, \ldots, y_m$.

$$AUC = \frac{1}{mn} \sum_{i=1}^{n} \sum_{j=1}^{m} H\left(x_i, y_j\right) \tag{2.6}$$

where $H(x_i, y_j) = \left\{1 \text{ if } x_i > y_j; \frac{1}{2} \text{ if } x_i = y_j; 0 \text{ if} x_i < y_j\right\}$. Moreover, the AUC is closely related to the ranking of the classification. All positive samples ranked higher than their negative counterparts, and AUC = 1. AUC indicates the probability of selection of a positive sample over a negative sample.

3 Results

3.1 Effect of dual-energy spectrum

To obtain optimal dual-energy images, various energy thresholds were set in the low-energy region based on the PCD system. The low-energy region was set at 22–23 keV, 24–25 keV, 26–27 keV,

28–29 keV, 30–31 keV. We evaluated the energy region with high contrast for microcalcifications in the low-energy region. Figure 1 shows the CNR evaluation for two types of microcalcifications according to the energy spectra. Although the CNR depends on the region-of-interest (ROI), the high CNR values were, on average, in the 26–27 keV region. In addition, the smaller size of microcalcifications makes it more difficult to distinguish the two types of microcalcifications because of the noise in the image. An ideal breast imaging should provide high contrast, resolution, and efficiency to detect breast lesions because of the low attenuation characteristic of X-rays. Therefore, the energy range threshold should be set properly for dual-energy acquisition. Based on figure 1, two energy bins were used, as presented in table 1. Case 1 included a high contrast of 26–27 keV in the high energy region, whereas Cases 2 and 3 were included in the low energy region. In PCD systems, dual-energy is acquired without overlapping the energy spectra, and the image quality is affected by the bin position and the width of the energy spectra [17]. Therefore, the wide width of the bin was set based on Case 2, and the narrow width of the bin was set based on Case 3 at low energy. Thus, selecting the appropriate energy bin combination is important because it affects the classification performance.

Figure 2 shows the classification of the two types of microcalcifications according to the energy combinations. The x-axis represents the score difference of the two microcalcifications, and the y-axis represents the score value of each microcalcification. The center of the samples is indicated by k-means clustering, which calculates the Euclidean distance of each sample [18]. As shown in figure 2(b), the classification performance was improved when a high contrast of 26–27 keV was included in the low-energy region. In addition, the classification performance was better in the wide width of the bin than in the narrow width of the bin. Thus, this result could provide an optimal compromise between the signal, noise, and detector electronics. These results indicate that the energy threshold for dual-energy image acquisition is important to discriminate between two similar materials [15]. Therefore, this classification exhibited better performance with high energy of 50 kVp and an energy threshold of 30 keV.

The classification performance was evaluated based on the dual-energy combination of the above-mentioned results using the simple-shaped and the XCAT phantoms (table 2). Figure 3 shows the results classified as a combination of a high energy of 50 kVp and an energy threshold of 30 keV. As shown in figure 3(a) and 3(b), the two curves are clearly separate, with only a little overlap. The simple phantom exhibited better performance because of its homogeneous background. Although microcalcifications are superimposed on dense breast tissue, as shown in figure 3(c) and 3(d), the XCAT phantom, which is modeled similar to the human breast, indicated the possibility of classification. Based on these results, the score values obtained using the dual-energy method can provide a quantitative evaluation indicator between the two types of microcalcifications.

Table 1. Specifications of dual-energy acquisition.

	Tube Voltage	Bin 1 (low-energy image)	Bin 2 (high-energy image)
Case 1	50 kVp	15–25 keV	26–50 keV
Case 2	50 kVp	15–30 keV	31–50 keV
Case 3	50 kVp	25–30 keV	31–50 keV

2020 JINST 15 C02033

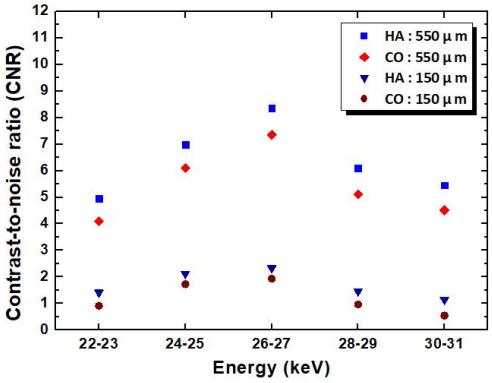

Figure 1. CNR evaluation using bin images obtained by setting various energy thresholds based on the PCD system. This figure represents two types of microcalcifications (HA: calcium hydroxyapatites, CO: calcium oxalate): the largest and the smallest.

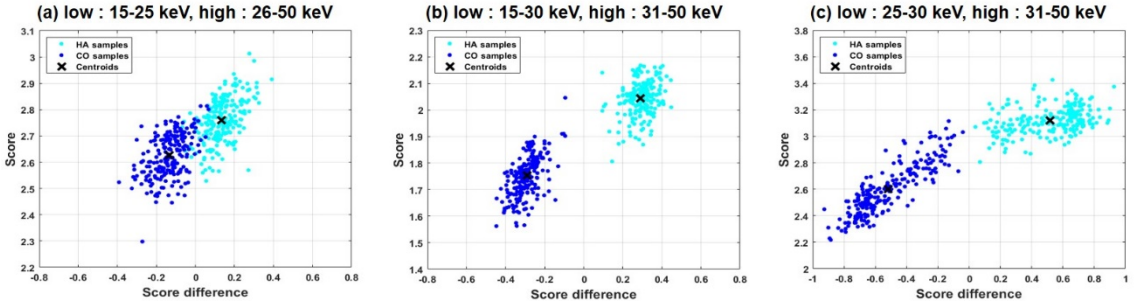

Figure 2. Assessment of classification according to energy combination (HA: calcium hydroxyapatites, CO: calcium oxalate). The x-axis represents the score difference of the two microcalcifications, and the y-axis represents the score value of each microcalcification. The center of the samples is indicated by k-means clustering, which calculates the Euclidean distance of each sample.

Table 2. Evaluation of the classification performance based on dual-energy combination.

	AUC performance	
Dual-energy combinations	Simple-shaped breast phantom	XCAT breast phantom
Case 1	0.89	0.79
Case 2	0.98	0.88
Case 3	0.97	0.86

3.2 Detection of malignant lesion

Based on the results obtained in section 3.1, only the malignant lesion can be automatically detected using the score obtained from the dual-energy image. Figure 4 shows a simple workflow that automatically displays only the calcium hydroxyapatite region. For this part of the study, we modeled a simulated breast phantom with two types of microcalcifications. In addition, we used a simple-phantom with a homogeneous background and an XCAT phantom with a heterogeneous background. Furthermore, the microcalcifications were modeled as either single or clustered, as shown in figure 5(a) and 5(b).

2020 JINST 15 C02033

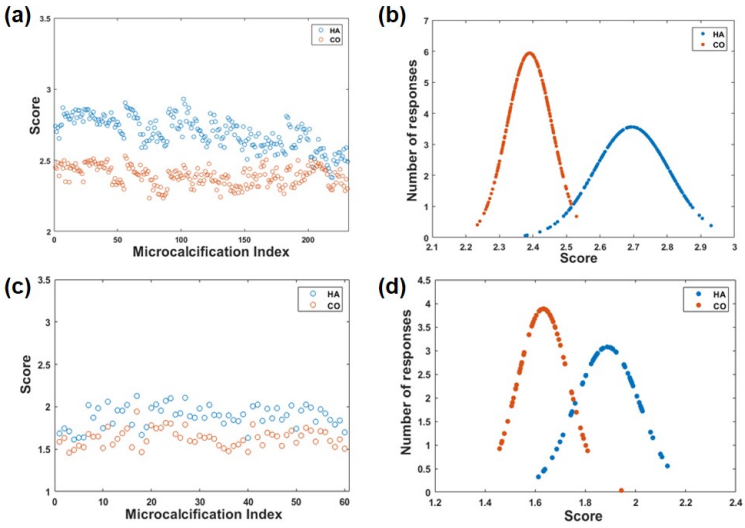

Figure 3. Evaluation of classification based on dual-energy combination using: (a) and (b) simple-shaped phantom, (c) and (d) XCAT phantom (HA: calcium hydroxyapatites, CO: calcium oxalate). (a) and (c) scatter plots show the classification scores of microcalcifications. (b) and (d) Gaussian distributions demonstrate the ability to distinguish between the two types of microcalcifications.

In figure 4, the dual-energy images are obtained (a), and all microcalcifications are detected using threshold-based segmentation (b). In this study, we used a segmentation technique based on the appropriate k-means clustering algorithm, which is one of the simplest methods to classify a given dataset according to the number of clusters. This method aims to minimize the sum of the distances of every pixel point in the cluster to the K center [18]. Because microcalcifications exhibit relatively high-intensity values in the image, the microcalcification region is separated from the breast image. After extracting the microcalcification region, the score values are calculated using the low- and high-energy images, as shown in eq. (2.4). Then, the pixel values of the microcalcification are converted into score values (c). The malignant lesion is segmented based on the minimum and maximum thresholds of the score obtained in the results in section 3.1 (figure 3(b) and 3(d)). The minimum and maximum thresholds can be set based on the score values obtained from the same geometry and energy spectrum [4]; then, only the malignant lesions can be extracted (d). Finally, the malignant lesion area is automatically displayed by bounding boxes using the region-growing segmentation (e). The seeded region growing method used in this study initially specifies one seed pixel and extends the size of the region to the neighboring pixels based on the intensity of the seed pixel [19]. As shown in figure 5, both the simple-shaped and the XCAT phantoms showed high performance.

4 Discussion

This study suggests two important points. First, we proposed a scoring method using the attenuation ratio to classify the microcalcifications associated with pathogenesis. This method is proposed as a quantitative analysis involving the discrimination criteria to classify malignant and benign lesions noninvasively. The comparison of score values of malignant and benign lesions is expected to be

2020 JINST 15 C02033

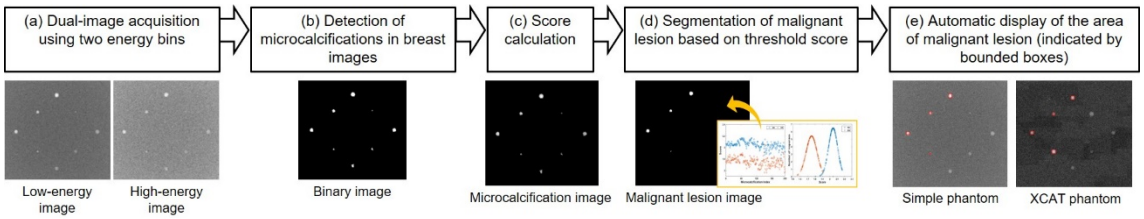

Figure 4. Flowchart showing the process of automatic displaying of the areas of calcium hydroxyapatites.

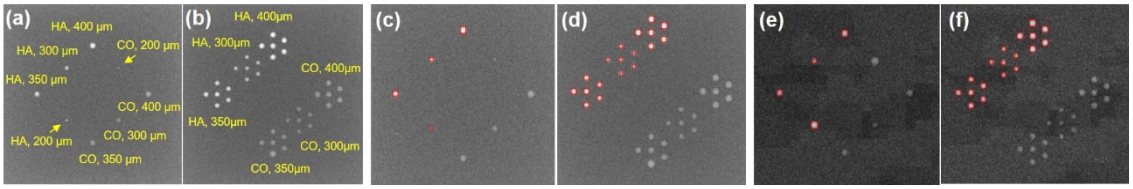

Figure 5. Simulated breast phantoms with two types of microcalcifications: (a) single and (b) cluster (HA: calcium hydroxyapatites, CO: calcium oxalate). Automatic displaying of the areas of malignant lesions (bounded box) using: (c) and (d) simple-shaped phantom, (e), and (f) XCAT phantom.

further improved based on large amounts of datasets obtained from the same system. However, the energy ranges to improve the classification performance should be set appropriately, as discussed in the results in section 3.1, because breasts exhibit a relatively large contrast difference in the low-energy region. In addition, spectral optimization for dual-energy is required for factors, such as breast type, detector characteristics, and X-ray system.

Second, to distinguish malignant and benign lesions in conventional mammograms, the morphological characteristics, such as the size, shape, number, cluster, and distribution, were used via a computer-aided diagnosis (CAD) system. As new approach, we suggested the possibility of automatic classification of malignant microcalcifications using segmentation methods and the minimum and the maximum thresholds of score values. Further, we demonstrated the possibility of classification using the XCAT breast phantom, whose structure is similar to that of actual breast tissues. However, because distinguishing the microcalcifications of dense tissues with high glandularity is difficult due to superposition, further research is required based on glandularity.

These analytical factors, which can be determined for malignant lesions, are expected to further improve the accuracy of early breast cancer detection. Furthermore, the proposed method requires an accurate detection of microcalcifications, and it calculates a score according to the pixel values of the microcalcification region. Thus, an improved classification performance is expected when using noise reduction methods for microcalcifications in image processing.

5 Conclusion

This study demonstrated the possibility of classifying microcalcifications based on a dual-energy method using mammograms, to determine whether microcalcifications are malignant or benign. We also confirmed that the two types of microcalcifications were distinguished by automatic

2020 JINST 15 C02033

classification using the score difference and the segmentation method. For improved performance, future studies are necessary to optimize the related parameters using more sample cases.

Acknowledgments

This research was supported by the Basic Science Research Program through the National Research Foundation of Korea (NRF) funded by the Ministry of Science, ICT & Future Planning (NRF-2017R1A2B2001818).

References

[1] P. Henrot, A. Leroux, C. Barlier and P. Génin, *Breast microcalcifications: The lesions in anatomical pathology*, *Diagn. Interventional Imaging* **95** (2014) 141.

[2] American College of Radiology, *ACR BI-RADS® ATLAS. Breast Imaging Reporting and Data System*, ACR (2013).

[3] L. Wilkinson, V. Thomas and N. Sharma, *Microcalcification on mammography: approaches to interpretation and biopsy*, *Br. J. Radiol.* **90** (2017) 20160594.

[4] H. Kim, M. Lee, D. Kim, D. Lee and H.-J. Kim, *Evaluation of photon-counting spectral mammography for classification of breast microcalcifications*, *Radiat. Phys. Chem.* **162** (2019) 39.

[5] B. Ghammraoui and S.J. Glick, *Investigating the feasibility of classifying breast microcalcifications using photon-counting spectral mammography: A simulation study*, *Med. Phys.* **44** (2017) 2304.

[6] M.P. Morgan, M.M. Cooke and G.M. McCarthy, *Microcalcifications associated with breast cancer: An epiphenomenon or biologically significant feature of selected tumors?*, *J. Mammary Gland Biol.* **10** (2005) 181.

[7] E. Fredenberg, M. Hemmendorff, B. Cederström, M. Aslund and M. Danielsson, *Contrast-enhanced spectral mammography with a photon-counting detector*, *Med. Phys.* **37** (2010) 2017.

[8] H. Ding, J.L. Ducote and S. Molloi, *Breast composition measurement with a cadmium-zinc-telluride based spectral computed tomography system*, *Med. Phys.* **39** (2012) 1289.

[9] H. Ding and S. Molloi, *Quantification of breast density with spectral mammography based on a scanned multi-slit photon-counting detector: a feasibility study*, *Phys. Med. Biol.* **57** (2012) 4719.

[10] T. Takahashi and S. Watanabe, *Recent progress in CdTe and CdZnTe detectors*, *IEEE Trans. Nucl. Sci.* **48** (2001) 950 [astro-ph/0107398].

[11] C.M. Li, W.P. Segars, G.D. Tourassi, J.M. Boone and J.T. Dobbins, *Methodology for generating a 3D computerized breast phantom from empirical data*, *Med. Phys.* **36** (2009) 3122.

[12] N. Kiarashi et al., *Development and application of a suite of 4-D virtual breast phantoms for optimization and evaluation of breast imaging systems*, *IEEE Trans. Med. Imaging* **33** (2014) 1401.

[13] https://www.hopkinsmedicine.org/radiology/research/divisions/radiological-physics/research/projects/imaging-simulation-computer-phantoms.html.

[14] J.H. Siewerdsen, A.M. Waese, D.J. Moseley, S. Richard and D.A. Jaffray, *Spektr: A computational tool for x-ray spectral analysis and imaging system optimization*, *Med. Phys.* **31** (2004) 3057.

[15] T.E. Kirkbride, A.Y. Raja, K. Müller, C.J. Bateman, F. Becce and N.G. Anderson, *Discrimination between calcium hydroxyapatite and calcium oxalate using multienergy spectral photon-counting CT*, *Am. J. Roentgenol.* **209** (2017) 1088.

2020 JINST 15 C02033

[16] C. Cortes and M. Mohri, *Confidence intervals for the area under the ROC curve*, in *Advances in Neural Information Processing Systems. Volume 17*, L.K. Saul, Y. Weiss and L. Bottou eds., MIT Press (2005), pp. 305–312.

[17] P.M. Shikhaliev, *Tilted angle CZT detector for photon counting/energy weighting x-ray and CT imaging*, *Phys. Med. Biol.* **51** (2006) 4267.

[18] A. Likas, N. Vlassis and J.J. Verbeek, *The global k-means clustering algorithm*, *Pattern Recognit.* **36** (2003) 451.

[19] M.M.S.J. Preetha, L.P. Suresh and M.J. Bosco, *Image segmentation using seeded region growing*, in *2012 International Conference on Computing, Electronics and Electrical Technologies (ICCEET)*, Kumaracoil, India, 21–22 March 2012, pp. 576–583.

2020 JINST 15 C02033